scientific data

OPEN

DATA DESCRIPTOR

An *in vivo* microscopy dataset for the characterization of leukocyte death

Alain Pulfer[1,2,9], Diego Ulisse Pizzagalli[1,3,9], Miguel Palomino Segura[4], Nina Germic[5], Tommaso Virgilio[1], Mauro Di Pilato[6], Pau Carrillo Barbera[7], Elisa Palladino[1], Paola Antonello[8], Marcus Thelen[1], Hans-Uwe Simon[5], Rolf Krause[3] & Santiago F. Gonzalez[1] ✉

Recent advancements in intravital microscopy have enabled the study of cell death *in vivo* under various experimental conditions, such as infection and cancer. However, the limited throughput of this technology, together with a lack of openly accessible datasets, affects the development of algorithms for the automatic detection and characterization of cell death, which in turn require the integration of extensive and curated datasets. To address these needs, we present a curated dataset of microscopy videos depicting the death of neutrophils, eosinophils, and dendritic cells, acquired in the spleen and in the lymph node of mice under inflammatory conditions. The dataset provides time-lapse imaging data, along with coordinates in space and time of cell death events displaying apoptotic–like morphodynamics, and 3D reconstruction of the cell morphology at each time point. Altogether, these data will be pivotal for developing computer vision and bioimage analysis methods to advance cell death research.

Background and Summary

Cell death is pivotal in multiple physiological and pathological processes[1,2]. Every day, damaged or dysfunctional cells undergo apoptosis to accommodate new healthy cells, an essential mechanism in tissue development and homeostasis[3–5]. Moreover, cell death is also associated with the defense mechanism entitled to clear dysfunctional or infected cells, thus preventing the onset of pathological conditions like cancer and infectious diseases[6]. The fine regulation of this mechanism is necessary to limit inflammation[7] and to prevent autoimmune disorders[2]. The death of immune cells is particularly important as it contributes to the initiation of the immune response[8], and the selection of antigen-specific cells[9], amongst others[10].

From a morphological perspective, multiple types of cell death are characterized by the disruption of the cell membrane and the formation of multiple bodies. Amongst these, apoptosis presents hallmarks such as chromatin condensation, cell shrinkage, membrane blebbing, and the formation of apoptotic bodies[11]. The latter are membrane vesicles that encapsulate the cytoplasm preventing the leakage of alarming signals into the extracellular space[12]. This process is considered immunologically silent, as it does not further elicit an inflammatory response. Successively, upon the formation of apoptotic bodies, phagocytic cells are recruited locally to clear the resulting apoptotic vesicles[13], promoting the end of this process. In this paper, we refer as "apoptotic-like" to all the cell death events that yield to the disruption of cell membrane and formation of apoptotic bodies.

Different imaging techniques can be used to study apoptotic-like cell death. *In vitro* imaging allows control over multiple experimental conditions, including cell density, migratory cues, or signaling pathways[14–16]. However, this modality cannot capture the complex behavior of the immune system within living tissues. Conversely, techniques such as 2-photon intravital microscopy (2P-IVM) enable the visualization of cells within their physiological

[1]Institute for Research in Biomedicine, Faculty of Biomedical Sciences, USI, Lugano, Switzerland. [2]Department of Information Technology and Electrical Engineering, ETH Zurich, Zurich, Switzerland. [3]Euler Institute, Faculty of Informatics, USI, Lugano, Switzerland. [4]Department of Physiology, Faculty of Sciences. Universidad de Extremadura, Badajoz, Spain. [5]Institute for Pharmacology, University of Bern, Bern, Switzerland. [6]Department of Immunology, University of Texas MD Anderson Cancer Center, Texas, USA. [7]Instituto de Biotecnología y Biomedicina (BioTecMed), Universitat de València, Valencia, Spain. [8]Department of Immunology, Weizman Institute of Science, Rehovot, Israel. [9]These authors contributed equally: Alain Pulfer, Diego Ulisse Pizzagalli. ✉e-mail: santiago.gonzalez@irb.usi.ch

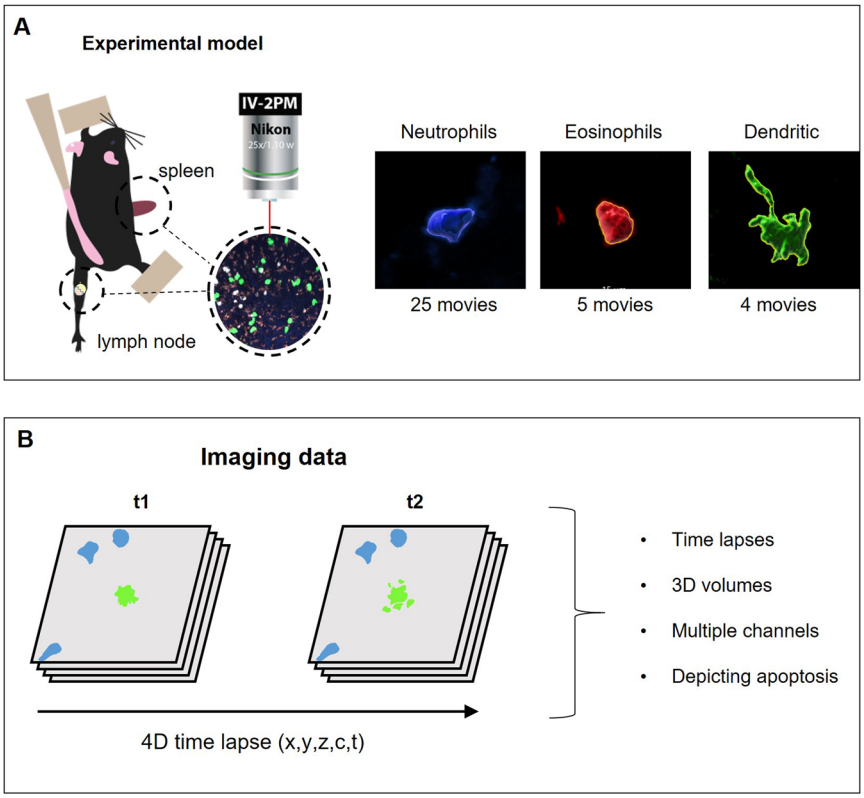

Fig. 1 Dataset generation workflow. (**A**) Representative intravital acquisition set-up. Immune-relevant tissues from an anesthetized mouse were surgically exposed and subjected to 2P-IVM. Resulting *in vivo* acquisitions (**B**) are 4D sequential data composed of multiple focal planes per time point and multiple channels. Raw data are annotated by three individual operators tracking cells undergoing apoptotic-like death and generating a 3D mask. Dying cells are associated with a cell state between "blebbing" and "disrupting" that defines the phase of the ongoing process.

environment by delivering in real time[17–19], four-dimensional time-lapses for different channels (x, y, z, c, t)[20,21]. Therefore, 2P-IVM represents one of the most informative platforms for the physiological study of cell death *in vivo*[22]. However, acquiring high-quality 2P-IVM movies remains non-trivial due to technical and biological challenges such as the surgical procedure, the bleaching of the sample, and the stability of the imaging site, among others[23–25]. As a result, the potential to generate extensive apoptotic datasets *in vivo* remains limited, whereas the lack of accessibility prevents the reuse of existing 2P-IVM movies[25,26]. Consequently, the scarcity of 2P-IVM movies negatively impacts studies that require curated datasets, such as comparative analysis or algorithmic solutions. This shortage of data mainly affects the latter aspect, given that mainstream deep learning (DL) algorithms are known for being data-hungry[27]. Therefore, establishing publicly accessible 2P-IVM repositories, complete with metadata and annotations, becomes pivotal. Such an initiative would broaden the scope of fundamental research on cell death and enable the development of robust algorithms to quantify this biological process *in vivo*.

In this study, we address this need by providing a comprehensive dataset capturing cell death events with apoptotic-like morphology *in vivo*[28]. This dataset encompasses 2P-IVM movies featuring three immune cell type:, neutrophils, eosinophils, and dendritic cells imaged in various experimental settings associated with the inflammatory response. A schematic workflow is shown in Fig. 1A,B. In addition to the raw data, we provide manual annotations of cell death events, which were curated by multiple operators trained to detect the morphological hallmarks of the process (Fig. 2). Accordingly, each apoptotic-like event is first identified in 2P-IVM fields-of-view (Fig. 2A), and successively annotated for the duration of the process (Fig. 2B). The annotations include centroid-based trajectories of the apoptotic-like events, frame-by-frame semantic annotations describing the cell morphology at any given time step, and 3D volumetric reconstructions of the cellular surface. To determine if a cell presented apoptotic-like morphology, we strictly adhered to the observation of the morphological hallmarks of apoptosis, including shrinkage of the cell, membrane blebbing, and the formation of apoptotic bodies. As a result, the presented catalog is an invaluable resource for comparative studies and the development of analytical solutions for the classification, detection, and segmentation of apoptotic-like cell death *in vivo*.

Methods

Mice. Mice were maintained in a pathogen-free animal facility at the Institute for Research in Biomedicine (Bellinzona, Switzerland). Before imaging, mice were anesthetized with a cocktail of xylazine (10 mg/Kg) and ketamine (100 mg/Kg), as previously reported[21]. All experiments were conducted in compliance with the regulations set by the local authorities and were approved by the Swiss Federal Veterinary Office.

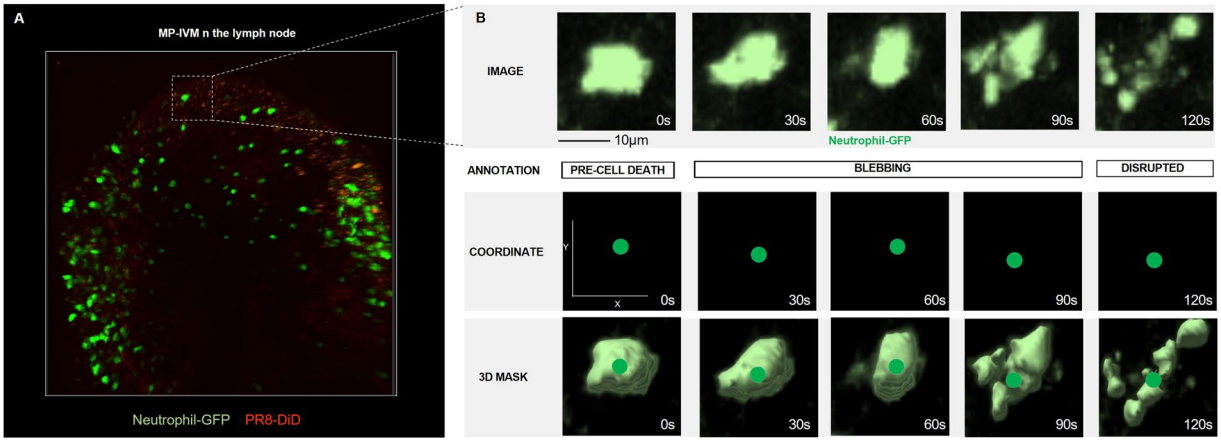

Fig. 2 Dataset annotation of apoptotic events. (**A**) Micrograph depicting a MP-IVM acquisition in the lymph node of a mouse. Neutrophils expressing GFP (green) and a UV-inactivated influenza vaccine are labeled with DiD (red). (**B**) Dying cells from MP-IVM acquisitions are annotated frame by frame for the duration of the process according to their morphology (top). Frame annotation include semantic labels (pre-apoptotic, blebbing, disrupted), centroid tracking (middle), and 3D volumetric reconstruction of the cell (bottom).

Intravital microscopy. All the videos were acquired through intravital two-photon microscopy (TrimScope, LaVision BioTec) in lymphoid organs (lymph nodes and spleen), under different experimental conditions detailed in Table 1. To acquire videos in the lymph nodes, the organ was exposed through minimally invasive surgery as previously described[29]. Then, time-lapse images were acquired using a custom upright microscope. To acquire videos in the spleen, mice were anesthetized and immobilized, while the spleen was accessed by making an incision through the skin and musculature as previously described[30]. After exposure of the organ, the spleen was moisturized by applying pre-warmed PBS. In both surgeries, 4D data encompassing multiple stacks, channels, and time points (Table 1, Fig. 1A) were generated. The imaging system employed two Ti:sapphire lasers (Chameleon Ultra I, Chameleon Ultra II, Coherent) and an optical oscillator that emitted light within the 1,010–1,340 nm range (Chameleon Compact OPO, Coherent). The output wavelength ranged between 690–1,080 nm, ontributing to probe excitation and tissue second-harmonic generation (SHG).

All the videos were acquired under inflammatory conditions. In all, except Neu7, Neu11, Neu17, and Den1, UV-inactivated PR8 virus was injected in the footpad 0 up to 24 hours prior to imaging. Neu7, Neu11, and Neu 17 videos were acquired in an experimental model of Vaccinia virus infection, whereas Den1 was acquired in a model of B16 melanoma metastasis in the lymph node. CFB and GFP-labeled neutrophils were adoptively transferred from a donor to a recipient animal which was CD11c-YFP in the case of Den1. Further details on the staining and experimental stimuli are available through Immunemap[31].

Data processing. The microscopy data acquired from the videos were stored in HDF5 files, comprising uint8 or uint16 TIFFs. Prior to image analysis, the raw data underwent no preprocessing. For cell detection, tracking, and volumetric reconstruction of the microscopy videos, we employed Imaris imaging software (Oxford Instruments, v9.7.2). Subsequently, the data obtained from Imaris underwent further analysis using customized Matlab and Python scripts (refer to the code availability section for details).

Manual tracking. The centroids of cells were manually annotated and tracked over time using the "Spots drawing" tool in Imaris (Bitplane). To ensure robustness, three operators independently and redundantly performed tracking without knowledge of reciprocal results. During the tracking process, the operators followed morphological criteria to identify cells showing apoptotic-like morphodynamics. Specifically, they focused on sequences exhibiting the characteristic hallmarks of apoptosis: 1) membrane blebbing, 2) subsequent formation of apoptotic bodies, and 3) eventual cell disruption (Fig. 2B). For each frame within the apoptotic-like sequences, the operators placed a centroid at the center of the cell using the Imaris "Spots" function, resulting in a connected track representing the apoptotic-like event (x, y, z, t, ID). Subsequently, the trajectories generated by each operator were consolidated into a ground truth using a majority consensus scheme that considered the duration and the location of the event. The starting and ending time points were determined by identifying overlaps among at least two of the three tracks of the annotators. For each time point, the two closest spatial coordinates were selected and averaged to create a final ground truth. Then, we performed volumetric 3D reconstruction using the Imaris "Surfaces" function. This reconstruction process generated precise 3D meshes of each cell undergoing apoptotic-like death, enhancing the accuracy and reliability of the dataset.

Semantic annotation. Three independent annotators labeled the state of the cells based on specific morphological criteria. To annotate the interval and dynamics of the cell death process, the annotators assigned to each cell, for each frame within the ground truth sequence, one of two semantic labels: "membrane blebbing" or "cell disruption (Table 2). To ensure robustness and consistency, a majority consensus scheme was employed to establish the final cell state. This scheme considered the overlap between annotations from at least two operators,

Video ID	CH1	CH2	CH3	CH4	Markers	Fluorophore	Organ	Stimuli	Objective
Den1	Den	Melanoma	Melanoma	—	CD11c, B16	EYFP, mCherry	Lymph node	melanoma	40x
Den2	Den	WT-Eos	KO Eos	—	not known, CK6, not specified	GFP, CMTMR, CFP	Spleen	UVPR8	40x
Den3	Den	Neu	SHG	—	CXCR3, Ly6G	GFP, CMTMR	Lymph node	UVPR8	40x
Den4	Den	NK	—	—	CD11c, NK1.1/NKp46	YFP, CMTMR	Lymph node	UVPR8	40x
Eos1	Den	WT Eos	KO Eos	—	CX3CR1, IL—5, IL-5	GFP, CMTMR, CTV	Spleen	UVPR8	16x
Eos2	Den	WT Eos	KO Eos	—	CX3CR1, IL-5, IL-5	GFP, CMTMR, CTV	Spleen	UVPR8	40x
Eos3	Den	WT Eos	KO Eos	—	CX3CR1, IL-5, IL-5	GFP, CMTMR, CTV	Spleen	UVPR8	40x
Eos4	Den	WT Eos	KO Eos	—	CX3CR1, IL-5, IL-5	GFP, CMTMR, CTV	Spleen	UVPR8	40x
Eos5	Den	WT Eos	KO Eos	—	CX3CR1, IL-5, IL-5	GFP, CMTMR, CTV	Spleen	UVPR8	40x
Neu1	Neu, NK	UVPR8	Neu, (follicle)	—	CK6, Ncr1, CD21/35	CFP, GFP, DiD, PB	Lymph node	UVPR8	20x
Neu2	SHG	UVPR8	—	Neu	LysM-Cre	CFP	Lymph node	UVPR8	40x
Neu3	Neu	Macro	UVPR8	—	LysM-Cre, CD169, UVPR8	GFP, PE, DiD	Lymph node	UVPR8	10x
Neu4	Neu	UVPR8	Neu, SHG	—	CK6	CFP	Lymph node	UVPR8	16x
Neu5	Neu	UVPR8	Neu, SHG	—	CK6	CFP	Lymph node	UVPR8	16x
Neu6	Neu	—	SHG	—	UBC	EGFP	Spleen	UVPR8	16x
Neu7	Naïve CD8 + T cell	Neu	Cognate CD8 + T cell	—	cell membrane, UBC	CMTMR, GFP, CTV	Spleen	None	16x
Neu 8	Neu	Macro	—	Neu, SHG	(reporter), CD169,	CFP, PE	Lymph node	UVPR8	40x
Neu 9	Neu	UVPR8	—	—	UBC	EGFP	Spleen	UVPR8	16x
Neu 10	Neu, Neu	UVPR8	Neu, SHG	—	CK6, UBC	CFP, GFP	Lymph node	UVPR8	16x
Neu11	Naïve CD8 + T cell	Neu	Cognate CD8 + T cell	—	cell membrane, UBC	CMTMR, GFP, CTV	Spleen	None	16x
Neu 12	Neu, DC	Neu	Neu	—	(reporter), CD11c, P2X7,	CFP, YFP, CMTMR	Lymph node	UVPR8	16x
Neu 13	FDC	—	—	Neu	8C12, (reporter)	Alexa fluor 568,CFP	Lymph node	UVPR8	20x
Neu14	Neu	UVPR8	SHG	—	UBC	EGFP	Spleen	UVPR8	16x
Neu15	Neu	UVPR8	SHG	—	UBC	EGFP	Spleen	UVPR8	16x
Neu16	Neu	—	SHG	UVPR9	UBC	EGFP	Spleen	UVPR8	16x
Neu 17	Neu	UVPR8	Neu	SHG	UBC, (cell membrane)	EGFP, Cell trace Far Red	Spleen	UVPR8	40x
Neu18	Neu	UVPR8	SHG	—	UBC	EGFP	Spleen	UVPR8	16x
Neu 19	Neu,DC	UVPR8	Neu, SHG	—	CK6, CD11c	CFP, YFP	Lymph node	UVPR8	40x
Neu 20	Dc	UVPR8	—	Neu	CD11c, (reporter)	YFP, CFP	Lymph node	UPPR8	40x
Neu 21	Neu	UVPR8	—	—	UBC	EGFP	Spleen	UVPR8	16x
Neu 22	Neu	UVPR8	—	—	UBC	EGFP	Spleen	UVPR8	16x
Neu 23	Neu	UVPR8	—	—	UBC	EGFP	Spleen	UVPR8	16x
Neu 24	Neu,DC	UVPR8	Neu, SHG	—	CK6, CD11c	CFP, YFP	Spleen	UVPR8	16x
Neu25	Neu	Den	—	SHG	CD11c, Ly6G	CMTMR, YFP	Lymph node	UVPR8	40x

Table 1. Experimental Conditions. This table details the channel specifications and experimental settings for each movie entry in the dataset. Cell types visible in each channel include neutrophils (Neu), dendritic cells (DCs), and eosinophils (Eos). Additionally, when applicable, the channels include second harmonic generation (SHG) and vaccine visualization. Experimental settings cover the used cell markers, fluorophores, target organ, applied stimuli, and microscope magnification.

promoting a unified and reliable consensus on the semantic label for each cell at every time point, hence minimizing potential biases and variations in the annotations.

Computation of quality metrics. To compute the signal-to-noise ratio (SNR) of the entries of the dataset, for each frame of the movies we computed a reference denoised image using a median filter. Successively, we used the SNR function of the Matlab Signal Processing toolbox to compare the reference image to the original one, computing an estimate of the SNR. This procedure was applied for each channel separately.

Computation of density metrics. The density metrics were computed using adaptive thresholding and morphological operations to separate foreground objects from the background in each channel. We then counted the number of cells visible at each time point in each channel. An estimate of the number of cells throughout the movies was generated by averaging these numbers over time. By knowing the spatial coordinates of the cells, we also estimated the average shortest distance between cells and a coefficient of clustering depicting the percentage of cells in close proximity.

Video ID	blebbing (start frame)	blebbing (end frame)	disruption (start frame)	disruption (end frame)	response (yes/no)	Channel
Neu1	3	5	6	10	yes	ch1
Neu2	18	20	21	22	no	ch1/ch4
Neu2	27	29	30	30	no	ch1
Neu2			24	30	no	ch1
Neu3			6	7	yes	ch1
Neu3	11	11	12	13	no	ch1
Neu4	9	11	12	15	no	ch1
Neu4	10	30	31	43	yes	ch1
Neu4	99	104	105	111	yes	ch1
Neu4			24	26	yes	ch1
Neu5	41	44	45	50	yes	ch1/ch3
Neu5	98	105	106	112	yes	ch1/ch3
Neu5	90	106	107	112	no	ch1/ch3
Neu6	17	18	19	23	no	ch1
Neu6			25	33	no	ch1
Neu6	37	53	54	60	no	ch1
Neu7			4	7	no	ch1
Neu7	21	24	25	26	no	ch1
Neu7	31	33	34	34	no	ch1
Neu7	43	43	44	51	no	ch1
Neu7	52	53	54	56	no	ch1
Neu7			53	57	no	ch1
Neu8	3	5	6	8	no	ch1/ch4
Neu9	25	25	26	30	no	ch1
Neu10			49	54	no	ch1/ch3
Neu11			1	3	no	ch1
Neu11			3	5	no	ch1
Neu11	20	21	22	24	no	ch1
Neu11			23	26	no	ch1
Neu11	24	24	25	29	yes	ch1
Neu11			26	28	no	ch1
Neu11	34	35	36	37	no	ch1
Neu11	36	37	38	40	no	ch1
Neu11	45	46	47	47	no	ch1
Neu11	51	52	53	55	no	ch1
Neu12	1	4	5	14	yes	ch1/ch3
Neu12			10	15	yes	ch1/ch3
Neu12	27	33	34	50	no	ch1/ch3
Neu12	46	49	50	54	no	ch1/ch3
Neu12	63	66	67	74	no	ch1/ch3
Neu12	104	129	121	124	yes	ch1/ch3
Neu12	145	146	147	150	no	ch1/ch3
Neu12	153	155	156	159	yes	ch1/ch3
Neu13	198	204	205	209	no	ch4
Neu13	247	252	253	255	no	ch4
Neu14	24	28	29	34	yes	ch1
Neu15	1	10	11	19	no	ch1
Neu16	2	6	7	14	yes	ch1
Neu16			19	22	yes	ch1
Neu16	28	41	42	45	yes	ch1
Neu17	111	111	112	114	yes	ch1
Neu18			1	12	yes	ch1
Neu18			28	33	no	ch1
Neu19	8	12	13	15	yes	ch1/ch3
Neu20	8	12	13	17	no	ch4/ch1
Neu20	22	25	26	34	no	ch4/ch1
Continued						

Video ID	blebbing (start frame)	blebbing (end frame)	disruption (start frame)	disruption (end frame)	response (yes/no)	Channel
Neu20			73	82	no	ch4/ch1
Neu20	103	104	105	108	yes	ch4/ch1
Neu21	1	5	6	12	no	ch1
Neu22			1	15	no	ch1
Neu23			11	17	no	ch1
Neu23			1	4	no	ch1
Neu24	7	8	9	12	no	ch1
Neu25	19	20	21	26	no	ch2
Eos1	1	34	35	52	no	ch3
Eos2	1	11	12	19	yes	ch1
Eos2			11	20	yes	ch3
Eos2	16	19	20	35	no	ch1
Eos2	15	29	30	47	no	ch1
Eos2	25	30	30	37	no	ch1
Eos2	1	5	6	10	yes	ch3
Eos3	1	6			yes	ch2
Eos3	18	31	32	40	yes	ch2
Eos3	24	33	34	36	no	ch2
Eos3	25	50	51	55	yes	ch2
Eos3	36	56	57	80	yes	ch2
Eos4	45	67	68	75	no	ch1
Eos4	49	71	72	81	no	ch1
Eos5	21	26	27	45	no	ch1
Den1	1	10	18	28	no	ch1
Den1	64	66	67	72	no	ch1
Den2			83	88	no	ch1
Den2	42	44	45	72	no	ch1
Den2	86	91	92	103	no	ch1
Den2	68	78	79	86	no	ch1
Den2	24	27	28	32	no	ch1
Den3			15	17	no	ch1
Den3	19	20	21	26	no	ch2
Den4			1	20	no	ch1
Den4	11	12	13	40	no	ch1

Table 2. Cell Death Phases Annotation. This table presents the semantic annotations of all cell death events. Each video entry includes a unique identifier along with frame-level semantic annotations indicating the morphological states of dying cells. The latter states are classified as "blebbing" or "disrupting," each characterized by a start and end frame. Additionally, the table indicates whether cell death events triggers a local immune response ("response").

Statistical analyses. Statistical analysis and plot visualization were performed using GraphPad Prism 8 (Graphpad, La Jolla, USA). All statistical tests were performed using the non-parametric Kruskal-Wallis test or Mann-Witney test. The significance of the p-value is described as * when $p < 0.05$, ** when $p < 0.01$, and *** when $p < 0.001$.

Data Record

Imaging data, metadata, and experimental details are available through the following channels: https://zenodo.org/records/14551288 or https://app.immunemap.org/cddb. The dataset on Zenodo[28] comprises unprocessed raw microscopy videos, each characterized by a unique identifier (ID) and essential metadata. These videos encompass multiple channels and extend across five dimensions: spatial coordinates (x, y, z), time (t), and multiple channels (c). Raw videos are stored in HDF5 format and uploaded individually according to their cell type, for instance "Neu1.h5". Within each HDF5 file, two types of annotations are included: 1) tracks coordinates of apoptotic-like events (x, y, z, t, ID), and 2) 3D volumetric reconstructions of cell deaths represented by meshes defined by vertices and edges. An additional folder labeled "Annotations" contains two sub-folders:

1. Cell deaths
2. Semantic annotations

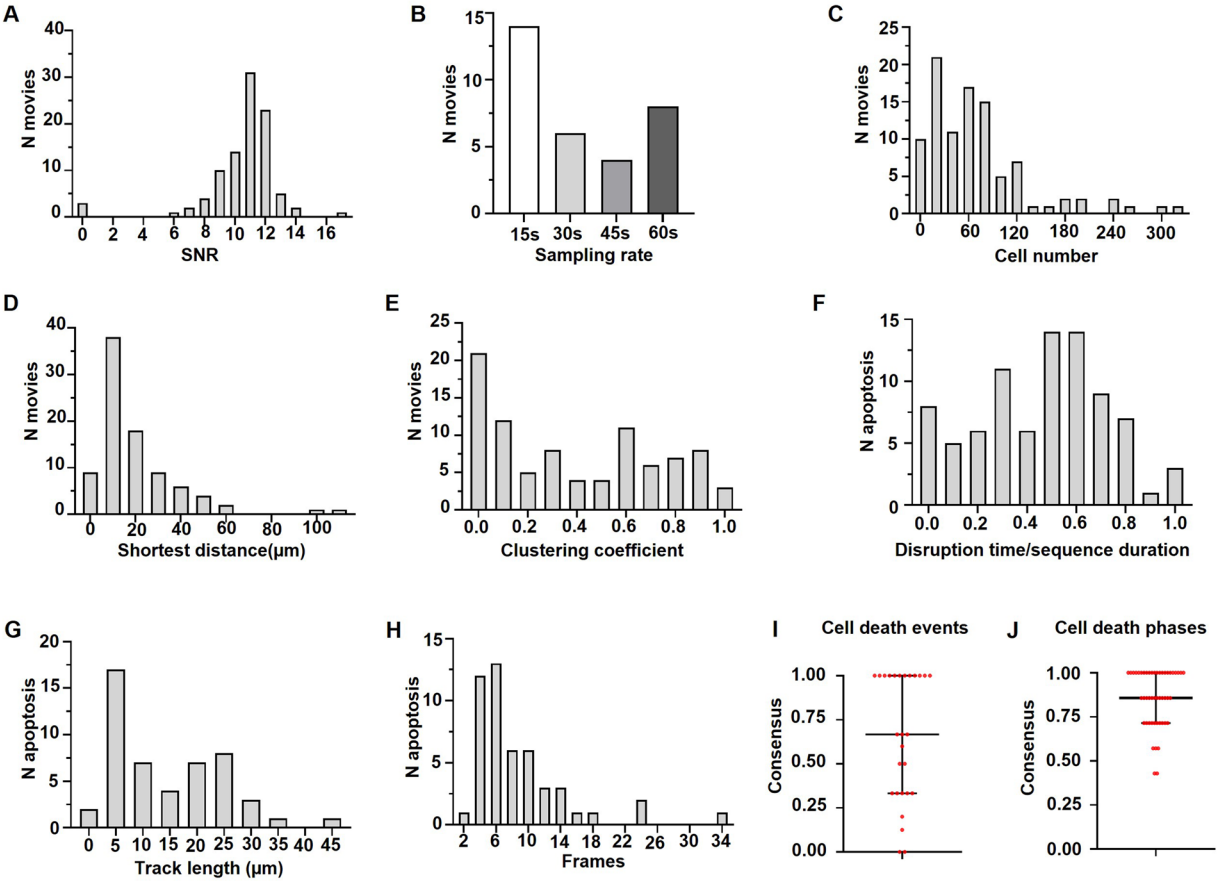

Fig. 3 Data quality and validation. (**A**) Distribution of the signal-to-noise ratio of the different movies. (**B**) Prevalence of the sampling rates used for different microscopy acquisition. (**C**) Distribution of cell number per field-of-view. (**D**) Distribution of the shortest distance between each cell. (**E**) Distribution of cells involved in a local cluster formed by at least three cells in close proximity. (**F**) Ratios between the annotated timing of cell disruption and sequence duration. A value of 0.5 indicates that the cell disrupts in the middle of the annotation. (**G,H**) Scatterplots showing the total track distance of annotated apoptotic-like events (**G**) and their duration in frames (**H**). (**I,J**) Inter-operator consensus rate during the annotation of apoptotic-like events (**I**) and phases (**J**).

The "Cell deaths" folder contains trajectories of apoptotic-like events in comma-separated value format (CSV). Each filename incorporates the identifier of the corresponding microscopy acquisition and the channel where apoptotic-like cells were observed, for instance "Neu1_ch1". The "Semantic annotations" folder contains semantic labels (CSV) describing the morphological state of cells at various stages of the cell death process. These labels indicate whether dying cells exhibit "blebbing" or "disruptive" morphology and if they elicit an immune response. Start and ending frames are provided to denote the time interval of each state. Lastly, three additional folders contain cropped microscopy movies centered around dying cells:

1. Dendritics_crops
2. Eosinophils_crops
3. Neutrophil_crops

Each cropped movie is named after the original uncropped acquisition and specifies the cell ID of the depicted cell death, such as "Neu1_cell1".

The dataset on immunemap[31] includes all the uncropped HD5F movies, providing complementary experimental details for each acquisition. In Supplementary Information we provide a minimal example in Python to download individual files using the Zenodo API. Moreover, data, metadata, experimental details and annotations (in JSON or CSV format) can be retrieved through the application programming interfaces offered by immunemap and described at https://www.immunemap.org/index.php/doc.

Technical Validation

Imaging acquisitions. Movies in the dataset were imaged with different microscopy settings. These included different voxel sizes, sampling rates, duration, and volume (Supplementary Table 3). As these parameters can influence the overall quality of the movies, we estimated the image quality of our dataset by computing the signal-to-noise (SNR) ratio for each acquisition (Fig. 3A). Higher SNR indicates better image quality, and reportedly,

values above five are considered sufficiently good to distinguish foreground objects from the background. Hence, the measured average SNR of 10 can assert the overall quality of the dataset and guarantee that their entries provide reliable and interpretable results.

The sampling rate of the movies in our dataset varied between 15, 30, 45, and 60 seconds (Fig. 3B). This aspect is relevant when evaluating dynamic processes in time lapses. Specifically, estimations of general cell motility, such as speed, straightness and cell tracking, can be significantly influenced by the selected sampling rate[23]. Lower sampling rates may result in the loss of critical information, especially in highly dynamic processes like cell death, where rapid and short-lived changes in the morphology of the cell may occur. To address this concern and ensure an accurate depiction of fast and transient processes, our dataset encompasses movies with high sampling rates.

Aside from the acquisition settings, the interpretability of imaging data can be influenced by the biological content and complexity of the acquisitions. A prominent parameter in this regard is cell density, which significantly impacts the analysis. In time lapses with high cell density, potential side effects, such as cluttering, cell merging, and cell splitting, may arise. These factors challenge cell detection efforts and may hinder crucial information within the data. Consequently, excessive cell density may render specific algorithms incapable of extracting meaningful insights from the movies. Therefore, we estimated pivotal parameters related to cell density and aggregation for each channel in the dataset. These parameters encompass the overall cell number, the shortest distance between cells, and a clustering coefficient that indicates the percentage of cells in close proximity to at least three other cells (Supplementary Table 3, Fig. 3C–E). These measurements underscore the variability in the dataset, with movies ranging from 20 cells to movies containing up to 300 cells and exhibiting a clustering coefficient near 1. By analyzing such diverse time-lapses, researchers can effectively benchmark their detection algorithms on increasingly complex scenarios, ensuring the robustness and applicability of their methods across a wide range of biological conditions and cell densities.

Apoptotic-like events. In the absence of specific apoptotic reporters, the annotated cells might follow a pathway different than apoptosis. For this reason, we adopt the umbrella term "apoptotic-like" to indicate all cell death events sharing morphological similarity with apoptosis. While this does not ensure the annotation of a specific death pathway, the presented catalogue is an invaluable resource for the development of analytical solutions for the classification, detection, and segmentation of cell death presenting apoptotic features *in vivo*. Cell death events with apoptotic-like hallmarks are inherently diverse, exhibiting variability that can affect classification and detection algorithms. One major challenge arises from the distinct morphologies of cells, leading to a class heterogeneity[32,33] that makes it difficult to identify consistent patterns within the same label in supervised classification. Additionally, the variable duration of sequences can pose a challenge to algorithms aimed at classifying the cell death process over time. Finally, the residual motility of cells, caused, for instance, by drifting, can further complicate the accurate identification of cell coordinates during the death process. To address these challenges and aid algorithm development, we estimated the variability between events in our dataset. We quantified the mean timing of cell disruption (Fig. 3F), which provides insights into the typical occurrence of this critical phase. Additionally, we assessed the average displacement of cells (Fig. 3G) and the overall duration of the disruption process (Fig. 3H), offering essential information to guide algorithmic solutions for cell death classification and detection. Hence, by considering these variabilities, researchers and practitioners can better design and fine-tune their algorithms for accurate classification and detection of apoptotic-like events.

Operator annotations. To assess the inter-operator variability during the annotation process, we introduced a consensus ratio, which quantifies the proportion of annotations that achieved agreement between at least two of the three operators involved. The mean consensus ratio for annotating apoptotic-like events was 0.6, indicating a moderate level of agreement among the operators and highlighting the intrinsic challenge of visually detecting apoptotic-like events based on morphological cues (Fig. 3I). However, when annotating the specific phases (Fig. 3J), the mean consensus ratio significantly increased to 0.9, reflecting the agreement between the operators in identifying the distinct phases.

Usage Notes

The proposed dataset represents a valuable resource for researchers seeking to characterize cell death. Cell biologists can utilize the presented dataset as a reference for the death of leukocytes *in vivo*, enabling the generation of pilot and comparative studies. In addition, they can gain valuable insights into different properties of the process, such as morphology, duration, and the recruiting of neighboring cells. A protocol for opening, downloading, and analyzing the dataset is provided in Supplementary Information and the code repository.

The heterogeneity of the videos included in this dataset (cell type, staining, organ, experimental conditions) should be considered in comparative studies. We recommend the users to always verify the physical parameters of the videos being compared, including volume and temporal sampling rate, as these can introduce a non-linear bias on metrics to quantify cellular morphodynamics such as cell speed. Moreover, the annotation of events relied exclusively on morphological hallmarks, without the usage of reporters for specific cell death modalities. While this is a major limitation of the study, as we cannot pinpoint the specific cell death modality, the dataset provides valuable information to develop computer vision-based methods for cell death quantification.

With access to the raw data and annotations, computer scientists can address the specific tasks of cell death classification, detection, and segmentation. To create a dataset for supervised-learning tasks, users can access the raw microscopy videos and their corresponding annotations provided in Excel format. By utilizing the annotations, it is possible to locate and track the centroids of individual apoptotic-like events over time (x, y, z, t). Using this information, users can define a suitable region around each cell to generate single-cell crops and the

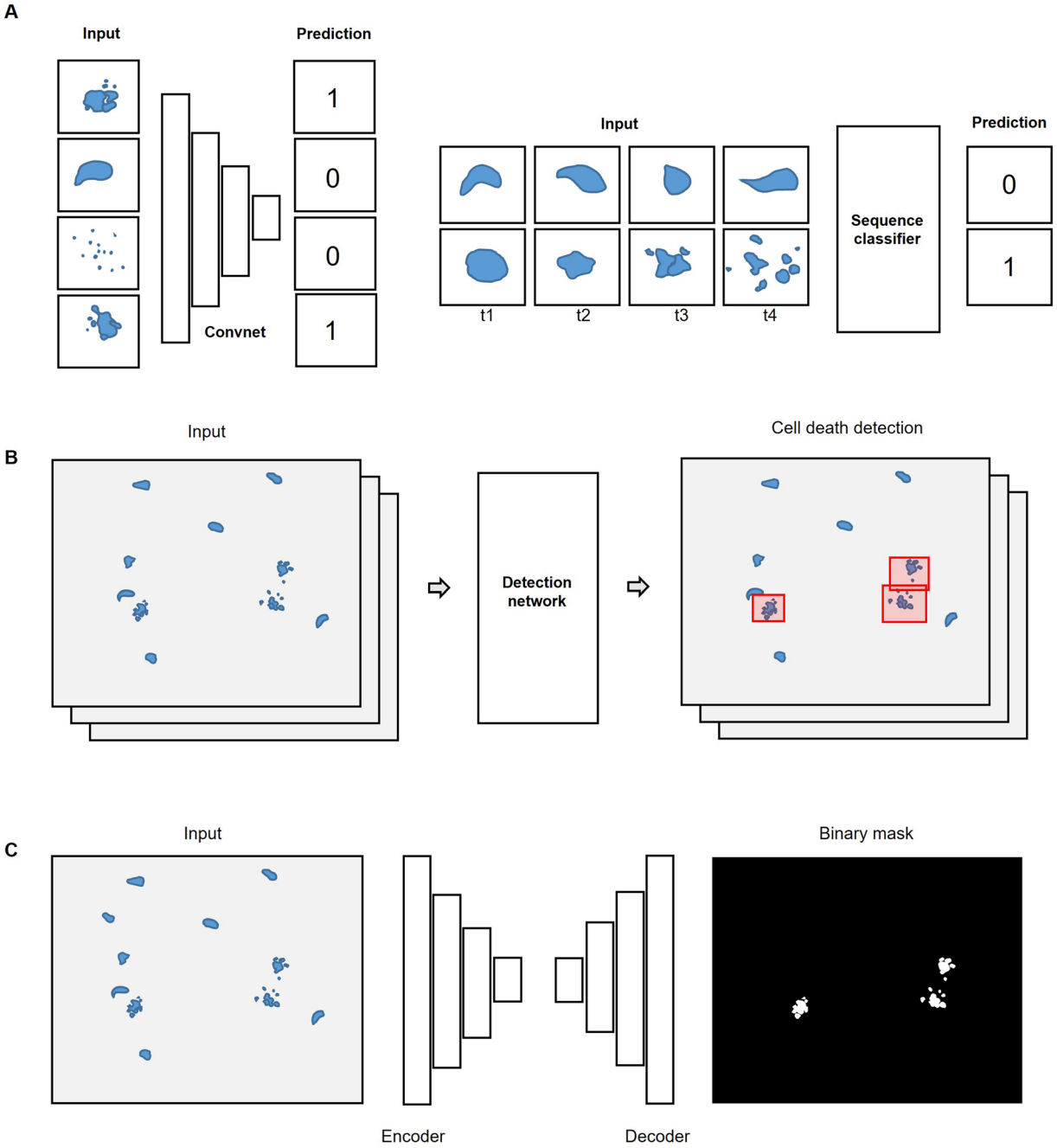

Fig. 4 Dataset usage for deep learning applications. (**A**) Schematic representation of the classification task applied to single image crops depicting dying cells (left) and to apoptotic-like sequences (right). Single image crops can be classified with the aid of convolutional networks, mapping an image to a corresponding binary value labelling healthy (0) or apoptotic-like (1) cells. Similarly, sequences images can be classified with activity recognition architectures. (**B**) Schematic depiction of a detection routine applied to full microscopy images containing healthy and dying cells. Input images are processed with a detector that predicts the spatial coordinates of apoptotic-like cells (red bounding boxes). (**C**) Schematic representation of the image segmentation task applied to full microscopy images depicting dying cells. Input microscopy images are processed with an auto encoder-decoder architecture which learns to map the input into a binary mask that highlights target cells only.

respective labels (0 for healthy, 1 for apoptotic). It is important to remark that identifying cell death events in this dataset relied on the analysis of video sequences. Therefore, we recommend that users analyze the entire temporal sequence.

The creation of personalized training datasets offers the possibility to train custom deep learning architectures for the classification of images depicting apoptotic-likw cells based on their morphology (Fig. 4A left). To accomplish this task, a wide array of deep learning architectures is available, such as convolutional networks

(CNNs)[34], capsule networks[35], and vision transformers[36,37], among others. Accordingly, recent studies demonstrated the successful classification of a variety of cell death types in static images[38,39]. Additionally, the presented dataset is best suited for the temporal classification of apoptotic-like sequences (Fig. 4A right), as the latter representation is expected to encapsulate more information than single-frame images. To this end, deep learning architectures tailored for activity recognition[40], such as 3DCNNs[41], recurrent networks[42], or optical flow-based methods[43], can be employed. Recurrent architectures have demonstrated effectiveness in classifying sequences acquired *in vitro*[1], showcasing their potential for this task. To achieve whole sequence classification, users can extract consecutive frames as cropped time-lapses, thus preserving the temporal dependencies of the events. With this information, users can train models capable of effectively analyzing the temporal dependencies and patterns exhibited by cells during cell death.

Users can tackle a task of increased complexity with respect to the classification problem by detecting dying cells within uncropped fields-of-view containing multiple cells (Fig. 4B). Accordingly, detecting apoptotic-like events amid other cells poses more significant challenges due to potential cell overlaps and background clutters[44]. Moreover, the temporal aspect of live cell imaging introduces new challenges, including morphological changes and sudden displacements. As a result, the algorithmic detection of cell death events in live cell imaging remains unexplored. To address this aspect, researchers can use the presented dataset to explore novel approaches for detecting apoptotic-like events in time-lapse microscopy.

Finally, the presented dataset is also suitable for cell segmentation (Fig. 4C) through the utilization of encoder-decoder architectures[45]. These DL networks have proven effective in several bio-imaging segmentation tasks, thus holding promising applications for segmenting cell death based on their morphology. In this regard, our dataset enables 3D and 2D cell segmentation by providing the 3D binary masks of the events over time. Consequently, researchers can apply 2D or 3D segmentation using each frame of the movies as an independent training sample.

Code availability

Code repository is available at: https://github.com/AlainPulfer/Leuko-Death.git.

The "Matlab code" folder contains functions to read acquisition data and annotations. The re-distributed "ImarisReader" (https://github.com/PeterBeemiller/ImarisReader) can read time-lapse acquisition stored within HDF5 files. The "getMask" function can retrieve the 2D and 3D masks of apoptotic-like events stored in the HDF5 files. The "signal2noise" function provides a measurement for the average and peak signal-to-noise in a specified channel of the acquisition (xyzct). The function "cellCount" estimates the average number of cells over time in a channel of interest. It additionally computes a mean distance between cells that is used to derive a clustering coefficient, which in turns measures the percentage of cells involved in local clusters.

The "LeukoDeath" folder provides different python functions to read, inspect, and display acquisition data as well as annotations. A detailed Jupiter Notebook illustrates how to use the source code to load movies into 2D and 3D Python arrays, manipulate these to access individual and sequential frames, and match the movie content with the respective annotations to generate datasets for classification tasks.

Received: 11 April 2024; Accepted: 12 February 2025;
Published online: 09 April 2025

References

1. Mobiny, A., Lu, H., Nguyen, H. V., Roysam, B. & Varadarajan, N. Automated Classification of Apoptosis in Phase Contrast Microscopy Using Capsule Network. *IEEE Transactions on Medical Imaging* **39**(1), 1–10, https://doi.org/10.1109/TMI.2019.2918181 (2020).
2. Elmore, S. Apoptosis: A Review of Programmed Cell Death. *Toxicologic Pathology* https://doi.org/10.1080/01926230701320337 (2007a).
3. Opferman, J. T. Apoptosis in the development of the immune system. In *Cell Death and Differentiation* (Vol. 15, Issue 2), https://doi.org/10.1038/sj.cdd.4402182 (2008).
4. Rathmell, J. C. & Thompson, C. B. Pathways of apoptosis in lymphocyte development, homeostasis, and disease. In *Cell* (Vol. 109, Issue 2 SUPPL. 1), https://doi.org/10.1016/S0092-8674(02)00704-3 (2002).
5. Elmore, S. Apoptosis: A Review of Programmed Cell Death. In *Toxicologic Pathology* (Vol. 35, Issue 4, pp. 495–516), https://doi.org/10.1080/01926230701320337 (2007b).
6. Hotchkiss, R. S., Strasser, A., McDunn, J. E. & Swanson, P. E. Mechanisms of disease: Cell death. *New England Journal of Medicine* **361**(16), 1570–1583, https://doi.org/10.1056/NEJMra0901217 (2009).
7. Yang, Y., Jiang, G., Zhang, P. & Fan, J. Programmed cell death and its role in inflammation. In *Military Medical Research* (Vol. 2, Issue 1), https://doi.org/10.1186/s40779-015-0039-0 (2015).
8. Chatziandreou, N. *et al*. Macrophage Death following Influenza Vaccination Initiates the Inflammatory Response that Promotes Dendritic Cell Function in the Draining Lymph Node. *Cell Reports*, **18**, https://doi.org/10.1016/j.celrep.2017.02.026 (2017).
9. Gonzalez, S. F. *et al*. Trafficking of B cell antigen in lymph nodes. *Annual Review of Immunology* **29**, 215–233, https://doi.org/10.1146/annurev-immunol-031210-101255 (2011).
10. Pérez-Figueroa, E., Álvarez-Carrasco, P., Ortega, E. & Maldonado-Bernal, C. Neutrophils: Many Ways to Die. In *Frontiers in Immunology* (Vol. 12), https://doi.org/10.3389/fimmu.2021.631821 (2021).
11. Tang, D., Kang, R., Berghe, T. V, Vandenabeele, P. & Kroemer, G. The molecular machinery of regulated cell death. In *Cell Research* (Vol. 29, Issue 5), https://doi.org/10.1038/s41422-019-0164-5 (2019).
12. Saraste, A.& Pulkki, K. Morphologic and biochemical hallmarks of apoptosis. In *Cardiovascular Research* (Vol. 45, Issue 3), https://doi.org/10.1016/S0008-6363(99)00384-3 (2000).
13. Doran, A. C., Yurdagul, A. & Tabas, I. Efferocytosis in health and disease. In *Nature Reviews Immunology* (Vol. 20, Issue 4), https://doi.org/10.1038/s41577-019-0240-6 (2020).
14. Isherwood, B. *et al*. Live cell *in vitro* and *in vivo* imaging applications: Accelerating drug discovery. In *Pharmaceutics* (Vol. 3, Issue 2). https://doi.org/10.3390/pharmaceutics3020141 (2011).
15. Kramer, N. *et al*. *In vitro* cell migration and invasion assays. In *Mutation Research - Reviews in Mutation Research* (Vol. 752, Issue 1), https://doi.org/10.1016/j.mrrev.2012.08.001 (2013).

16. Pijuan, J. *et al*. *In vitro* cell migration, invasion, and adhesion assays: From cell imaging to data analysis. *Frontiers in Cell and Developmental Biology*, **7**(JUN). https://doi.org/10.3389/fcell.2019.00107 (2019).
17. Grootveld, A. K. *et al*. Apoptotic cell fragments locally activate tingible body macrophages in the germinal center. *Cell*, **186**(6). https://doi.org/10.1016/j.cell.2023.02.004 (2023).
18. Mayer, C. T. *et al*. The microanatomic segregation of selection by apoptosis in the germinal center. *Science*, **358**(6360), https://doi.org/10.1126/science.aao2602 (2017).
19. Mesa, K. R. *et al*. Niche-induced cell death and epithelial phagocytosis regulate hair follicle stem cell pool. *Nature*, **522**(7554), https://doi.org/10.1038/nature14306 (2015).
20. Secklehner, J., Lo Celso, C. & Carlin, L. M. Intravital microscopy in historic and contemporary immunology. In *Immunology and Cell Biology* (Vol. 95, Issue 6), https://doi.org/10.1038/icb.2017.25 (2017).
21. Sumen, C., Mempel, T. R., Mazo, I. B. & Von Andrian, U. H. Intravital microscopy: Visualizing immunity in context. In *Immunity* (Vol. 21, Issue 3), https://doi.org/10.1016/j.immuni.2004.08.006 (2004).
22. Kranich, J. *et al*. *In vivo* identification of apoptotic and extracellular vesicle-bound live cells using image-based deep learning. *Journal of Extracellular Vesicles*, **9**(1), https://doi.org/10.1080/20013078.2020.1792683 (2020).
23. Beltman, J. B. *et al*. Analysing immune cell migration. *Nature Reviews. Immunology* **9**(11), 789–798, https://doi.org/10.1038/nri2638 (2009).
24. Pizzagalli, D. U. *et al*. Data Descriptor: Leukocyte Tracking Database, a collection of immune cell tracks from intravital 2-photon microscopy videos. *Scientific Data* **5**, 1–13, https://doi.org/10.1038/sdata.2018.129 (2018).
25. Sinaci, A. A. *et al*. From Raw Data to FAIR Data: The FAIRification Workflow for Health Research. *Methods of Information in Medicine*, **59**(6), https://doi.org/10.1055/s-0040-1713684 (2020).
26. Jacobsen, A. *et al*. A generic workflow for the data fairification process. *Data Intelligence*, **2**(1–2), https://doi.org/10.1162/dint_a_00028 (2020).
27. Adadi, A. A survey on data-efficient algorithms in big data era. *Journal of Big Data*, **8**(1), https://doi.org/10.1186/s40537-021-00419-9 (2021).
28. Pulfer, A. *et al*. An *in vivo* microscopy dataset capturing leukocyte cell death. *Zenodo* https://doi.org/10.5281/zenodo.14551288 (2025).
29. Masedunskas, A. *et al*. Intravital microscopy: A practical guide on imaging intracellular structures in live animals. *BioArchitecture*, **2**(5), https://doi.org/10.4161/bioa.21758 (2012).
30. Di Pilato, M. *et al*. Neutrophil subtypes shape HIV-specific CD8 T-cell responses after vaccinia virus infection. *Npj Vaccines*, **6**(1), https://doi.org/10.1038/s41541-021-00314-7 (2021).
31. Pizzagalli, D. U. *et al*. *Systematic analysis of immune cell motility leveraging Immunemap, an open intravital microscopy atlas*. https://doi.org/10.1101/2024.12.02.626343 (2024).
32. Pang, G., Shen, C., Cao, L. & Van Den Hengel, A. Deep Learning for Anomaly Detection: A Review. In *ACM Computing Surveys* (Vol. 54, Issue 2), https://doi.org/10.1145/3439950 (2021).
33. Van Valen, D. A. *et al*. Deep Learning Automates the Quantitative Analysis of Individual Cells in Live-Cell Imaging Experiments. *PLoS Computational Biology*, **12**(11), https://doi.org/10.1371/journal.pcbi.1005177 (2016).
34. Bhatt, D. *et al*. Cnn variants for computer vision: History, architecture, application, challenges and future scope. In *Electronics (Switzerland)* (Vol. 10, Issue 20), https://doi.org/10.3390/electronics10202470 (2021).
35. Kwabena Patrick, M. *et al*. Capsule Networks – A survey. In *Journal of King Saud University - Computer and Information Sciences* (Vol. 34, Issue 1), https://doi.org/10.1016/j.jksuci.2019.09.014 (2022).
36. Han, K. *et al*. A Survey on Vision Transformer. *IEEE Transactions on Pattern Analysis and Machine Intelligence*, **45**(1), https://doi.org/10.1109/TPAMI.2022.3152247 (2023).
37. He, K. *et al*. Transformers in medical image analysis. In *Intelligent Medicine* (Vol. 3, Issue 1), https://doi.org/10.1016/j.imed.2022.07.002 (2023).
38. Jin, J. *et al*. Machine Learning Classifies Ferroptosis and Apoptosis Cell Death Modalities with TfR1 Immunostaining. *ACS Chemical Biology*, **17**(3). https://doi.org/10.1021/acschembio.1c00953 (2022).
39. Verduijn, J., Van der Meeren, L., Krysko, D. V. & Skirtach, A. G. Deep learning with digital holographic microscopy discriminates apoptosis and necroptosis. *Cell Death Discovery*, **7**(1), https://doi.org/10.1038/s41420-021-00616-8 (2021).
40. Yeole, C., Singh, H., Waykole, H. & Deshpande, A. Deep Neural Network Approaches for Video Based Human Activity Recognition. *International Journal of Innovative Science and Research Technology*, **6**(6) (2021).
41. Vrskova, R., Hudec, R., Kamencay, P. & Sykora, P. Human Activity Classification Using the 3DCNN Architecture. *Applied Sciences (Switzerland)*, **12**(2), https://doi.org/10.3390/app12020931 (2022).
42. Mohd Noor, M. H., Tan, S. Y. & Ab Wahab, M. N. Deep Temporal Conv-LSTM for Activity Recognition. *Neural Processing Letters*, **54**(5), https://doi.org/10.1007/s11063-022-10799-5 (2022).
43. Weinzaepfel, P., Revaud, J., Harchaoui, Z. & Schmid, C. DeepFlow: Large displacement optical flow with deep matching. *Proceedings of the IEEE International Conference on Computer Vision*. https://doi.org/10.1109/ICCV.2013.175 (2013).
44. Vrigkas, M., Nikou, C. & Kakadiaris, I. A. A review of human activity recognition methods. In *Frontiers Robotics AI* (Vol. 2, Issue NOV), https://doi.org/10.3389/frobt.2015.00028 (2015).
45. Ronneberger, O., Fischer, P. & Brox, T. U-net: Convolutional networks for biomedical image segmentation. *Lecture Notes in Computer Science (Including Subseries Lecture Notes in Artificial Intelligence and Lecture Notes in Bioinformatics)*. https://doi.org/10.1007/978-3-319-24574-4_28 (2015).

Acknowledgements

Swiss National Science Foundation grants 176124 (A.P., D.U.P., M.P., T.V., S.G.), 310030_163336 (P.A., M.T.), SystemsX.ch 2013124 (D.U.P., R.K., S.G.), Biolink 189699 (S.G., D.U.P., P.C.B., E.P.), swissuniversities RE2VITAL grant (S.F.G., R.K., D.U.P., A.P., E.P.), USI FIR (D.U.P.).

Author contributions

Conceptualization: A.P., D.U.P., S.G.; Methodology: A.P., D.U.P.; Experiments: M.P., N.G., T.V., M.D.P., P.A., D.U.P., S.G.; Data annotation: A.P., D.U.P., P.C.B., T.V., P.A.; Data analysis and visualization: A.P.; Figures: A.P., D.U.P.; Writing original draft: A.P., P.C.B., D.U.P., S.G.; Revision: A.P., D.U.P., E.P., S.G.

Competing interests

The authors declare no competing interests.

Additional information

Supplementary information The online version contains supplementary material available at https://doi.org/10.1038/s41597-025-04632-6.

Correspondence and requests for materials should be addressed to S.F.G.